Title

Nonlinear elasticity and short-range mechanical coupling govern the rate and symmetry of mouth opening in Hydra

Journal

Proceedings of the Royal Society B, 291(2017)

ISSN

0962-8452

Authors

Goel, Tapan

Adams, Ellen M

Bialas, April L

et al.

Publication Date

2024-02-28

DOI

10.1098/rspb.2023.2123

Peer reviewed

PROCEEDINGS OF
THE ROYAL SOCIETY B
BIOLOGICAL SCIENCES

Non-linear elasticity and short-range mechanical coupling govern the rate and symmetry of mouth opening in Hydra

Journal:	*Proceedings B*
Manuscript ID	RSPB-2023-2123.R1
Article Type:	Research
Subject:	Biophysics < BIOLOGY, Behaviour < BIOLOGY, Neuroscience < BIOLOGY
Keywords:	epithelium, viscoelastic, chimera, strain hardening, nearest-neighbor interaction
Proceedings B category:	Behaviour

Author-supplied statements

Relevant information will appear here if provided.

Ethics

Does your article include research that required ethical approval or permits?:

Statement (if applicable):
This research uses the freshwater invertebrate Hydra and therefore does not require IACUC approval.

Data

It is a condition of publication that data, code and materials supporting your paper are made publicly available. Does your paper present new data?:

Statement (if applicable):
This paper involves new data generated in laboratory experiments and a computational model. Both, the data and the code associated with the manuscript have been deposited to Zenodo at: https://doi.org/doi:10.5281/zenodo.10498855

If yes, please tell us how your data or code can be accessed and provide a link to your data if it is in a repository for the editors and reviewers to use.
CUST_DATA_INITIAL_ACCESS :No data available.

If your data is in a repository, please provide any temporary (private) link/s for reviewers/editors to access here.
CUST_REPOSITORY_LINKS :No data available.

Conflict of interest

I/we declare we have no competing interests.

Statement (if applicable):
CUST_STATE_CONFLICT :No data available.

Use of AI

Please provide a statement of any use of AI technology in the preparation of the paper.

No, we have not used AI-assisted technologies in creating this article

CUST_IF_YES_DECLARATION_OF_AI_USE :No data available.

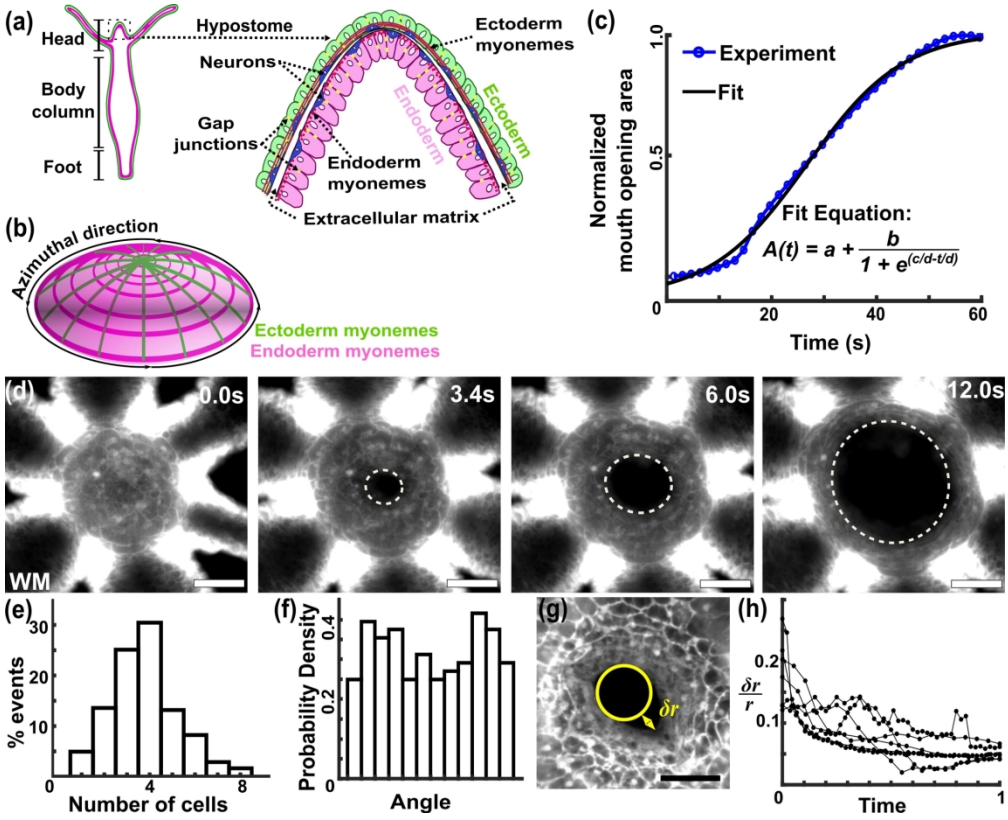

Figure 1: Hydra head anatomy and mouth opening dynamics. (a) Schematic showing basic Hydra anatomy and cell types including a zoomed-in cross-section of the hypostome. (b) Schematic top-down view of the myoneme organization in the ectoderm (green) and endoderm (magenta) in the Hydra head. (c) Area of the mouth (normalized to the maximum area) as a function of time. The blue curve shows representative experimental data. The black curve corresponds to a logistic fit as described by the equation on the right. 'a', 'b', 'c' and 'd' correspond to the minimum normalized area, maximum normalized area, time to reach half maximum and timescale of mouth opening respectively. (d) Still images from Movie S1 showing quinine hydrochloride (0.5 mM) induced opening of the ectodermal epithelial layer in a Watermelon (WM) Hydra (scale bar: 100 μm). (e) Histogram of number of cells involved in each tugging event (n = 364 tugging events from N = 8 independent events). (f) Probability density function for the relative angle between successive tugging events (n = 184 tugging event pairs from N = 5 independent mouth opening events). (g) Representative image of a radial tug during mouth opening induced by 0.2mM reduced glutathione (scale bar: 200 μm). (h) Time evolution of the relative fluctuation of the mouth radius, δr/r, averaged over the azimuth (N = 6 mouth opening events). Time is normalized from the beginning of mouth opening to when the mouth reaches its maximum area.

198x160mm (300 x 300 DPI)

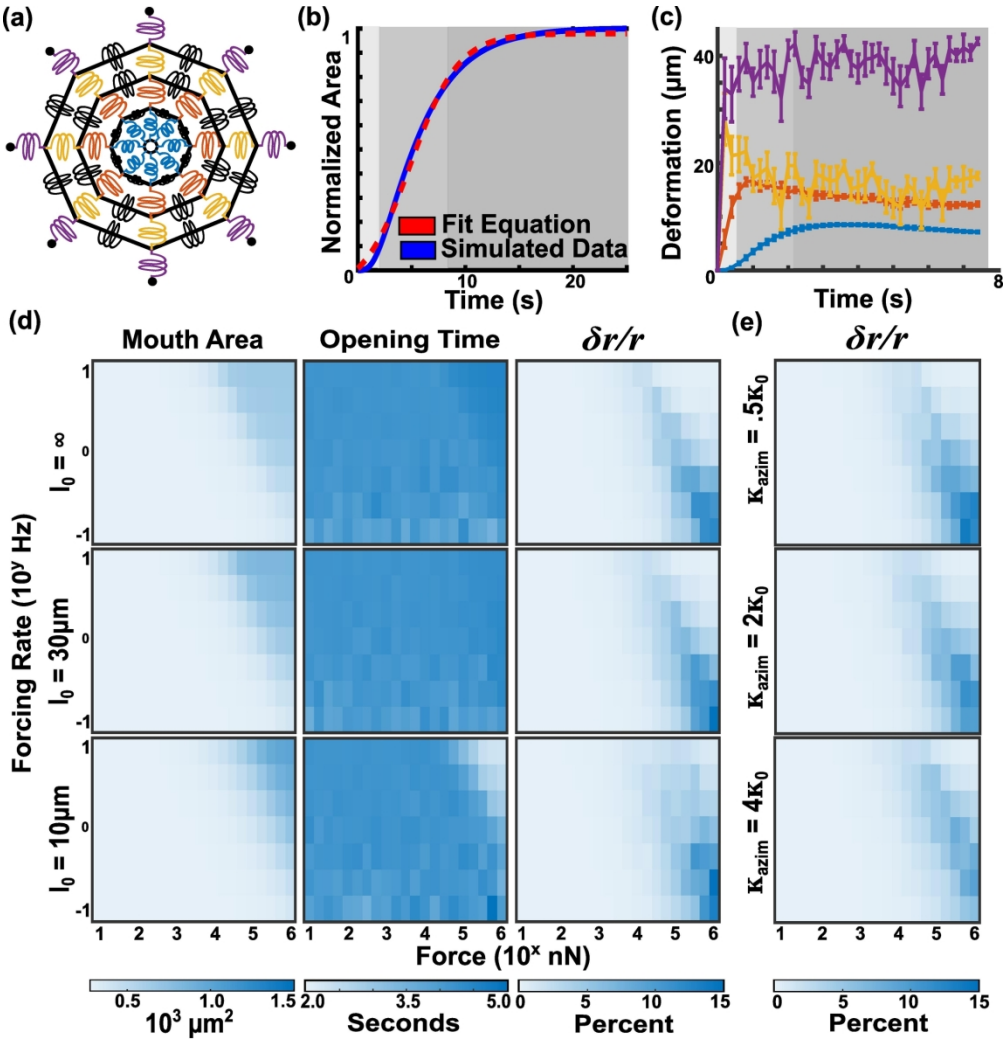

Figure 2: Non-linear spring network model captures macroscopic features of mouth opening. (a) Schematic of the spring network. Color-coding indicates distance from center. (b) Comparison between mouth opening time series obtained from model simulations (blue) and the logistic curve fit (red). Intensity of grey background denotes phases of mouth opening (from light to dark): slow increase, fast increase, and saturation. (c) Azimuthally averaged radial deformation of vertices in each N-gon. Line colors match those of the radial springs in (a). Grey background matches that of (b). (d) Variation of final mouth area (left column) fitted mouth opening time (middle column), and relative fluctuations in mouth radius, δr/r (right column), as functions of the active force strength (x-axis) and the average forcing rate (y-axis) for different non-linear regimes: without non-linearity (top), weak non-linearity (middle) and strong non-linearity (bottom). Note the axes have logarithmic scales. A darker blue color indicates larger mouth areas (left), longer opening times (middle) and larger relative fluctuations in mouth radius (right). (e) Changes in relative fluctuations in mouth radius with changes in the stiffness of the azimuthal springs relative to stiffness of radial springs (κ0). l_0=30 μm for all three heat maps. Parameters for all simulations along with descriptions and relevant sources can be found in Table S1.

190x196mm (300 x 300 DPI)

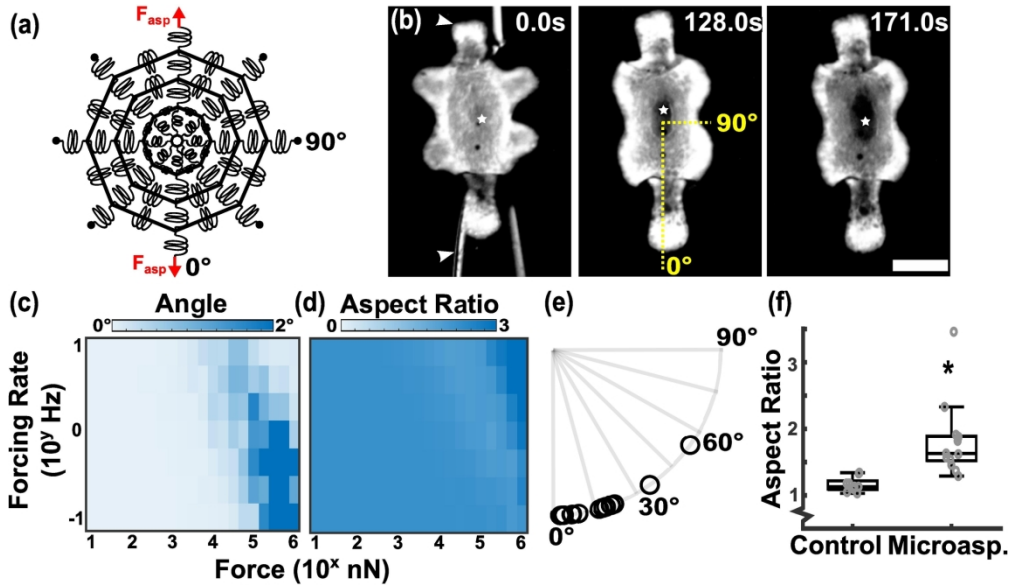

Figure 3: Application of external uniaxial tension affects symmetry of mouth opening. (a) Schematic of the hypostome under uniaxial tension. Fasp is the strength of the microaspiration force. (b) Still image sequence of mouth opening when the head is placed under uniaxial tension by applying negative pressure. Arrowheads indicate the location of needles used to apply negative pressure on the head. Star indicates the mouth opening (Scale bar: 100 μm). (c) Orientation angle of major axis (relative to the direction of tensile force) and (d) aspect ratio of best fit ellipse to the mouth, in simulations, as functions of the strength and rate of the active force (l_0=20μm). (e) Orientation angle of major axis (relative to the direction of tensile force) (N = 13) and (f) aspect ratio of best fit ellipse to the mouth, from experiments (N = 9 (Control), N = 13 (Microaspirated)). (*) indicates p-value = 0.0006 for a one-tailed two-sample Student's t-test.

189x110mm (300 x 300 DPI)

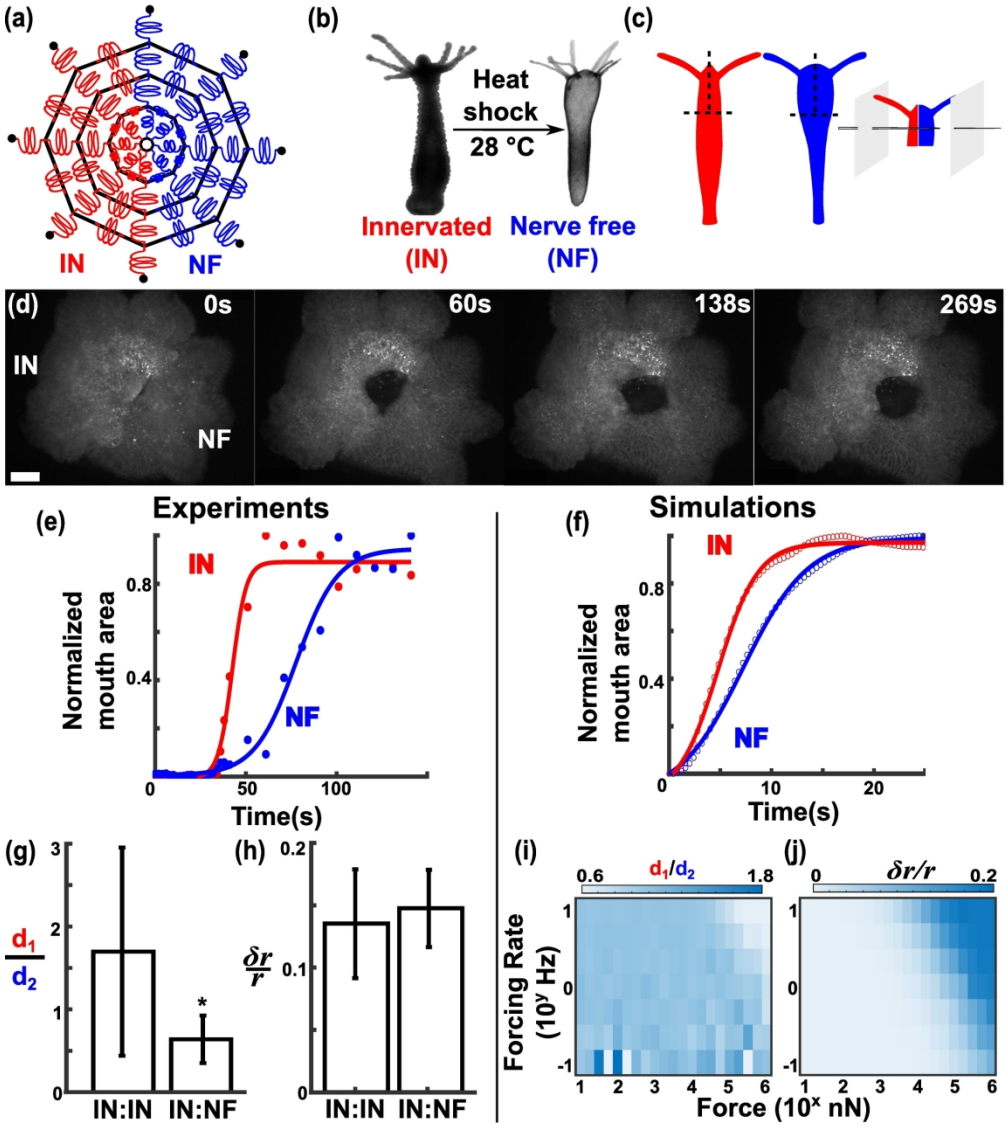

Figure 4: The nerve-net is required to initiate but not to execute mouth opening. (a) Schematic of the simulated chimera. (b) Greyscale images of innervated and nerve-free Hydra generated by heat shock treatment of the A10 strain. Note the nerve-free animal is more bloated at the oral end due to buildup of fluid. (c) Schematic showing the process of creating chimeras. (d) Still image sequence of mouth opening in an innervated:nerve-free chimera (scale bar: 100 μm). Representative mouth area-time curves (e) in vivo and (f) in silico. Comparison of the (g) ratio of mouth opening times and (h) relative fluctuations in mouth radius between control chimeras (N = 6) and innervated:nerve-free chimeras (N = 9). (*) denotes p-value < 0.05 (i) Ratio of mouth opening times and (j) relative fluctuations in mouth radius for innervated:nerve-free chimeras, in simulations, as functions of the strength and rate of the active force in the strongly non-linear regime (l_0=10μm). Simulation parameters provided in Table S1.

190x213mm (300 x 300 DPI)

Non-linear elasticity and short-range mechanical coupling govern the rate and symmetry of mouth opening in *Hydra*

Tapan Goel[1], Ellen M. Adams[3], April L. Bialas[3], Cassidy M. Tran[2], Trevor Rowe[1], Sara Martin[3], Maia Chandler[4], Johanna Schubert[4,] Patrick H. Diamond[1], Eva-Maria S. Collins[1,3,4*]

[1] Department of Physics, University of California San Diego, La Jolla, CA, 92093, USA

[2] Division of Biological Sciences, University of California San Diego, La Jolla, CA, 92093, USA

[3] Department of Biology, Swarthmore College, Swarthmore, PA, 19081, USA

[4] Department of Neuroscience, Perelman School of Medicine, University of Pennsylvania, Philadelphia, PA, USA

***Corresponding Author**

Eva-Maria S. Collins

Email: ecollin3@swarthmore.edu (E-MSC)

Keywords: epithelium; viscoelastic; chimera; strain hardening; nearest-neighbor interaction

Abstract

Hydra has a tubular bilayered epithelial body column with a dome-shaped head on one end and a foot on the other. Hydra lacks a permanent mouth: its head epithelium is sealed. Upon neuronal activation, a mouth opens at the apex of the head which can exceed the body column diameter in seconds, allowing Hydra to ingest prey larger than itself. While the kinematics of mouth opening are well characterized, the underlying mechanism is unknown. We show that Hydra mouth opening is generated by independent local contractions that require tissue-level coordination. We model the head epithelium as an active viscoelastic non-linear spring network. The model reproduces the size, timescale, and symmetry of mouth opening. It shows that radial contractions, travelling inwards from the outer boundary of the head, pull the mouth open. Non-linear elasticity makes mouth opening larger and faster, contrary to expectations. The model correctly predicts changes in mouth shape in response to external forces. By generating innervated:nerve-free chimera in experiments and simulations, we show that nearest-neighbor mechanical signaling suffices to coordinate mouth opening. Hydra mouth opening shows that in the absence of long-range chemical or neuronal signals, short-range mechanical coupling is sufficient to produce long-range order in tissue deformations.

Introduction

Epithelial tissues experience extreme deformations, such as bending, stretching, and compression. Withstanding these deformations is essential for maintaining tissue integrity and physiological function. Mouth opening in the freshwater cnidarian *Hydra* is a physiologically relevant process to examine the role of extreme deformations for epithelial tissue function. *Hydra* lacks a permanent mouth and creates a new mouth opening in the apex of its head epithelium every time it needs to feed, egest, or vent fluid from its body cavity. A previous study (1) revealed the kinematics of *Hydra* mouth opening (**Figure 1**): a) The mouth area grows as a logistic function of time (S-shaped curve) over seconds to tens of seconds, b) the initial mouth opening is asymmetric but as opening progresses the circularity of mouth opening increases, and c) the mouth opening is due to extreme cell deformations, with azimuthal cell strains of up to 200% and no cell rearrangements (1) (**Figure S1** and **Movie S1)**. This behavior is in contrast to the large-scale tissue

deformations observed during development which rely on cell migration on minute to hour long timescales (2). Thus, as reviewed in (3), *Hydra* mouth opening is an excellent *in vivo* system to study how cell-level deformations give rise to organismal level behaviors.

Hydra consists of a cylindrical body column, about 1 cm long and a few hundred microns in diameter, with a foot at one end and a dome-shaped head surrounded by a ring of tentacles at the other end **(Figure 1a)**. As a cnidarian, *Hydra* lacks a mesoderm: it is composed of two epitheliomuscular cell layers, an outer ectoderm and inner endoderm, separated by an extracellular matrix (ECM) (**Figure 1a**). The epithelial cells have epitheliomuscular processes (myonemes) that originate from the basal side of the epithelial cells and extend into the ECM (4). Individual myonemes only span over 1-2 cells (4–6). However, when visualized using phalloidin staining, myonemes appear as long fibers on a tissue scale (1). In the endoderm, myonemes are organized in concentric circles in both body column and the head **(Figure 1b)**. Ectodermal myonemes are organized perpendicular to endodermal ones: They run parallel to the oral-aboral axis in the body column and appear as radial spokes in the head **(Figure 1b**) (1,4–6). Treatment with 2.5% (w/v) magnesium chloride ($MgCl_2$), a muscle relaxant used for jelly fish (7), blocked both longitudinal body column contractions and mouth opening and it was shown that the endoderm starts opening only after the ectoderm has opened to a critical area (1). Based on these observations, it was proposed that the active contraction of ectodermal myonemes generate the forces necessary for mouth opening (1). However, how cell-level myoneme contraction is coordinated to cause the S-shaped opening kinematics **(Figure 1c)** and symmetric mouth opening **(Figure 1d)** is unknown.

This study integrates previous and new experimental observations for a mechanistic understanding of mouth opening. Using fluorescence imaging of different transgenic *Hydra* lines, we deduce the length- and timescales of the "individual" (cell-level) deformations produced by local myoneme contractions and the spatiotemporal pattern of myoneme activation in the head. With this information, we develop a non-linear, viscoelastic spring network model of the *Hydra* head. Despite its simplicity, the model captures the main macroscopic features of mouth opening in *Hydra.* It can also predict changes to these macroscopic features in response to perturbations, which we have experimentally tested. Because the model uses only a few parameters that can be experimentally constrained, we can develop a physical intuition for the mouth opening process and gain new biological insights.

Results and Discussion

It has been shown that the mouth opening is less circular initially and becomes more circular over time (1). This initial asymmetry likely arises from local myoneme activity. Ectoderm cells are about 20 μm in diameter and individual ectodermal myonemes range between 5-20 μm in length (4). Thus, they generate short-range contractile forces. These short-range forces act across neighboring cells to generate 'tugs' – radial tissue deformations at the mouth perimeter involving 3-4 adjacent cells (**Figure 1e**), on the order of ~70-90 μm (compared to a radius of ~200 μm of the head). The angles between successive tugs, binned into 100 ms intervals, are distributed uniformly (**Figure 1f**, p-value = 0.87, two-sample Kolmogorov Smirnov test against a uniform distribution), showing that the tugs are azimuthally uncorrelated. These uncorrelated tugs lead to the initial non-circularity of the mouth that has previously been reported (1). Despite this lack of azimuthal coordination at short timescales, mouth opening is radially symmetric over long timescales of tens of seconds: relative fluctuations in the (azimuthally) averaged mouth radius decrease over the course of mouth opening and settle to about 5% (**Figure 1g,h**). This implies that local deformations are spatially synchronized to achieve the observed symmetric mouth opening. Note that very large openings that lead to endoderm evagination, as sometimes observed with chemical induction or during feeding (1,8), are not considered in our analysis.

While transgenic *Hydra* lines exist for imaging myonemes *in vivo* (9), the large-scale tissue deformation of mouth opening prevents the resolution of individual myonemes **(Figure S2)**. However, because *Hydra's* epitheliomuscular cells require intracellular calcium (Ca^{2+}) for contraction, we can visualize the spatio-temporal pattern of calcium in the epithelial tissue using genetically encoded Ca^{2+} indicators (GCaMP6s) and thus obtain the spatio-temporal pattern of active contractile forces (10–12). This allowed us to determine

whether the initial active forces are localized within a specific region of the head. Previous work using low magnification lateral imaging of transgenic *Hydra* that express the GCaMP6s in the ectodermal epithelial layer suggested that epithelial cell activity begins at the center of the mouth and propagates outward as mouth opening continues (10,13). We performed both low-resolution lateral and high-resolution top-down imaging of heads of *Hydra* expressing GCaMP6s in the ectoderm. Mouth opening was induced via exposure to quinine or reduced glutathione (1,14), which bind to receptors in sensory neurons (15,16). The neurons are thought to activate epithelial cell contraction using neuropeptides (12,17,18). Upon stimulation, variations in Ca^{2+} signaling across the head were observed (**Figure S3**). However, consistent Ca^{2+} activity was seen along the base of the *Hydra* head near the tentacle ring at the onset of mouth opening in all 16 top-down and in 7/9 of all sideview movies (**Figure S3,** SI Section 1.1 and **Movie S2**). Thus, myoneme contractions at the head boundary appear to induce opening.

The active contraction of ectodermal myonemes generate the forces necessary for mouth opening, while the endoderm follows with the same logistic kinematics for the opening area with a time delay (1). In this study, we focus on the dynamics after both epithelia have opened. Because active forces are only being produced in the ectoderm, the passive mechanical response of the tissue can be effectively captured by modifying the elastic modulus and viscosity of a single layer. Further, because out-of-plane deformations are limited (Methods), we can model the head epithelial tissue as a 2D network of coupled non-linear springs (**Figure 2a, S1b**), representing both epithelial layers and the ECM. Since neuronal signals are required to trigger mouth opening (19,20), they are incorporated as sources that generate active forces.

The network of non-linear springs is arranged in R+1 concentric regular N-gons (polygons with N vertices) (**Figure 2a**). For simplicity, we present results for a model using 5 concentric octagons (see **Figure S5** for other cases of R and N). Each vertex is connected to its four nearest neighbors by non-linear springs, except the vertices on the innermost and outermost octagon. All vertices are movable, except for those in the $(R+1)^{th}$ -octagon, which represents a fixed boundary – the tentacle ring at the base of the head. The spring network represents the elastic behavior of the coupled epithelial tissue layers and not myonemes or individual cells. Since mouth opening is a low Reynolds number process ($Re = \frac{\rho l v}{\eta} \sim 10^{-10}$), we ignore the inertial term in the momentum balance equations describing the motion of the vertices. The forces produced by the ectodermal myonemes are represented by short-lived "external" radial forces acting on the vertices in the network.

Guided by the experimental data, we make two more assumptions: 1) At timescales > 100 ms, the active forces generated by the radial myonemes can be treated as uncorrelated, and 2) the active forces, act only on the head boundary, because Ca^{2+} activity was always observed at the boundary in experiments (**Figure S1a, Figure S3,** Supplementary Appendix Section 1.1 and **Movie S2**). Therefore, we model the active forces as independent Poisson processes and we constrain them to only act on the vertices of the R^{th} polygon, in the radially outward direction (See Figure S4 and Supplementary Appendix Section 1.1 for results corresponding to activation in the center). The dynamical equations for the vertices of the non-linear spring network under these assumptions (see Methods), primarily depend only on two adjustable parameters: the ratio of the strength of the active force to the strength of the characteristic elastic force of the non-linear springs ($\frac{\tilde{f}_0}{\kappa l_0}$) and the ratio of the rate of active forcing to the viscoelastic relaxation rate ($\frac{\lambda\kappa}{\mu}$). Using published data, we estimated κ and μ (**Table S1**). Because the forces exerted by individual myonemes are unknown, we varied the active forcing rate λ and the active force strength $\tilde{f}_0$, over several orders of magnitude to investigate how the macroscopic behavior of the system would change across a wide range of parameters. We also varied the strength of non-linear elasticity in the model by changing l_0 to understand how changes in the mechanical properties of the epithelial tissue might affect the macroscopic features of mouth opening.

Mechanical cascade generates the logistic (S-shape) mouth area-time curve

The model reproduces the experimentally observed logistic time curve (defined in **Figure 1c**) for the mouth area (**Figure 2b**). The slow initial increase of the mouth area is caused by a cascade of tissue deformations (**Figure 2c**): The active forces at the head boundary act at random timepoints on the outermost $(R)^{th}$ ring of

vertices causing the outermost set of radial springs to contract. This transmits force to the springs connecting the $(R-1)^{th}$ and R^{th} polygons, causing them to pull on the vertices in the $(R-1)^{th}$ polygon. This transmits forces to the springs connecting the $(R-2)^{th}$ and $(R-1)^{th}$ polygons, causing them to pull on the vertices in the $(R-2)^{th}$ polygon, and so on. Thus, force is transmitted from the outermost to the innermost ring with a time delay as the springs contract sequentially. This is seen in the time shift between the peak deformation of the springs in the outermost and those in the innermost ring (**Figure 2c**) and creates the observed slow initial increase of the mouth area curve. Once the outer springs reach their steady state lengths – effectively functioning as rigid rods transmitting force to the inner vertices – the mouth area increases quickly. The mouth area saturates once the elastic restoring forces of the springs equal the strength of the stochastic active forces. When this point is reached, the active forces only produce transient local deformations that undergo very fast viscoelastic relaxation, and the mouth area remains constant (plateau in **Figure 2b,c**). This mechanism of a deformation cascade differs from the hypothesis proposed in (1) that the initial dynamics are a result of increasing active myoneme forces (See Supplementary Appendix Section 1.2).

The non-linearity facilitates wider and faster mouth opening

The model shows that the mouth area increases with increasing strength and increasing rate of the active force (**Figure 2d (Left)**). As the total amount of work done by the active forces on the tissue increases, either through increasing the magnitude of the force or its frequency, an increased amount of elastic energy is stored in the spring network resulting in a larger mouth opening. The non-linear elastic term $\left(\frac{1}{l_0}\right)$ makes the springs stiffer as they deform. Strain stiffening has been reported for a variety of biological materials in response to mechanical perturbation (21–24). With increased stiffness, one would expect tissue deformations to be smaller because stiffer tissue requires a greater force to be deformed to the same extent as less stiff tissue. However, for a given active force strength and forcing rate, as the strength of non-linearity increases, the mouth area increases (**Figure 2d (Left)**): as the non-linearity increases, more force is transferred from the outer springs to the inner springs for the same deformation of the outer springs, resulting in larger mouth opening (see Supplementary Appendix Section 1.3). In addition, the timescale of mouth opening showed a functional change in its response to the strength and rate of the active force, depending on the strength of the non-linearity (**Figure 2d (Middle)**). Without non-linearity ($l_0 = \infty$) the spring stiffness is constant, and the opening time increases with the strength and the rate of the active forcing. For intermediate values of the non-linear coefficient ($l_0 = 30$ μm), the timescale of mouth opening is insensitive to the active force. In the strongly non-linear regime ($l_0 = 10$ μm), the timescale of opening decreases as the strength and rate of the active force increases. Thus, for the same strength and rate of active forcing, the timescale of mouth opening reduces as the non-linearity increases (for a detailed explanation, see Supplementary Appendix Section 1.3).

Nearest-neighbor coupling controls the symmetry of mouth opening

The model reproduces the radial symmetry of mouth opening that is experimentally observed. The measure of asymmetry of the mouth radius, the relative fluctuations in mouth radius ($\delta r/r$), is on the order of 5% for most of the parameter space explored, in agreement with experiments **(Figure 1h, 2d (Right))**. To understand how this symmetry arises despite the uncorrelated stochastic forces, we modified the model by increasing the stiffness of the azimuthal springs (black springs in Figure **2a**), keeping everything else constant. The increased stiffness caused a reduction in the relative fluctuations in radius ($\delta r/r$), i.e., an increase in symmetry (**Figure 2e**). This symmetry increase can be attributed to the nearest neighbor coupling of the vertices by springs. When an individual vertex moves radially due to a short-lived active force, the azimuthal springs connecting it to its neighbors pull it back to its original position and distribute some of that force to the neighbors. This decreases the asymmetry caused by the active force (for a detailed explanation, see Supplementary Appendix Section 1.4).

Because the tentacle ring acts as a circular boundary of the head epithelium, we had assumed that the vertices on the outer boundary of the spring network are stationary – imposing a fixed circularly symmetric boundary condition on the spring network. To investigate the role of this boundary condition regarding mouth opening symmetry, we simulated the response of the spring network to a constant uniaxial force. The uniaxial force caused the head boundary to distort from a circular to an elliptical shape during the mouth opening process.

In simulations, we accomplished this by adding a constant radial force to a pair of diametrically opposite vertices that were originally constrained to be stationary **(Figure 3a)** The shape of the mouth opening was quantified by measuring the aspect ratio (the ratio of the major axis length to the minor axis length) and major axis orientation of the best fit ellipse to the mouth. The model predicted that the major axis of the ellipse should align with the direction of the uniaxial tension (**Figure 3c**) and that the aspect ratio of the ellipse should exceed 1 across a range of active forces and forcing rates (**Figure 3d**).

We tested these predictions experimentally by recording mouth opening in *Hydra* heads subjected to constant uniaxial tension generated by microaspiration (**Figure 3b**, **Figure S6**, **Movie S3**) and found qualitative agreement. The measured aspect ratio of the microaspirated mouth opening (1.8 ± 0.6, mean ± standard deviation, N = 13 microaspirated heads) was significantly larger ((p-value = 0.0006, one-tailed two-sample Student's *t*-test) than that of the control (1.2 ± 0.1, N = 9 control heads) (**Figure 3f**). The major axis of the ellipse was closely aligned to the direction of the uniaxial force (angle between uniaxial force and major axis of best fit ellipse to the mouth = $16.5 \pm 14.9°$, mean ± standard deviation, N = 13 microaspirated heads) (**Figure 3e**). Thus, the model correctly predicted how the shape of the head boundary affects the shape of the mouth opening.

To verify that mechanical nearest neighbor interactions were sufficient for mouth opening in the real system, we tested mouth opening behavior in nerve-free chimera and in *Hydra* in which we pharmacologically blocked gap junction communication to prevent the exchange of ions and small molecules between cells.

Nerve-free *Hydra* (19,25) cannot open their mouths (20,26). Sensory neurons initiate mouth opening by activating the ectodermal epitheliomuscular cells that pull the mouth open. In our model we assume that once activated by a neuronal signal, signal propagation is mechanical and thus does not require a nervous system. Supporting this assumption, we found that nerve-free *Hydra* open their mouths upon electrical stimulation (**Movie S4**). This suggests that the nerve net is only necessary to trigger mouth opening.

We could not use electrical stimulation to quantify the kinematics of mouth opening in nerve-free *Hydra* due to the size of the electrode being comparable to the size of the *Hydra* head. Therefore, to investigate whether the nerve net affected opening kinematics, we took advantage of *Hydra*'s unique regenerative properties and created chimeric animals with a nerve net in only half of the head, i.e., innervated:nerve-free *Hydra* (**Figure 4a-c, S6a**). To account for possible effects from the grafting, we compared the behavior to innervated:innervated *Hydra* chimera. We also simulated the chimeric innervated:nerve-free *Hydra* using our model: we set the active forces to zero on half of the vertices in the outermost polygon, creating a "semi-circular" passive sector of the network (**Figure 4a**). In both simulations and experiments, we found that upon activation (chemical stimulation with quinine in experiments) (**Movie S5**) only the innervated half of the chimeric head deformed initially, and the mouth started opening initially only in the innervated half (**Figure 4d-f**), whereas in innervated:innervated *Hydra* mouth opening occurred in both halves. After a short delay, the nerve-free part of the innervated:nerve-free *Hydra* head also deformed, albeit slower than the innervated half (**Figure 4d-f**), creating a more symmetric final mouth opening (**Figure 4h,j**). The mouth areas associated with innervated and nerve-free halves both showed the logistic time dependence observed in control (innervated:innervated) *Hydra*. The ratio of the timescale of mouth opening ($\frac{d_{innervated}}{d_{nerve-free}}$) in experiments was significantly lower (p-value = 0.03 Student's *t*-test) for the innervated:nerve-free chimeras (ratio = 0.64 ± 0.29 (mean ± standard deviation), n = 9 movies, N = 9 chimeras) compared to control (innervated: innervated) chimeras (ratio = 1.70 ± 1.26, n = 8 movies, N = 6 chimeras) (**Figure 4g**). The ratio of the timescales obtained from the simulations in the strongly non-linear regime was the same order of magnitude as seen in the experiments (**Figure 4g, i**). Thus, both simulations and experiments with innervated:nerve-free chimeras suggest that non-neuronal cellular communication suffices for the propagation of mouth opening and produces the logistic opening kinematics.

Hydra ectodermal cells are connected via gap junctions (27) and gap junctions have been found to control other large-scale shape changes that are due to ectodermal myoneme contraction, such as body column shortening (28,29). Therefore, we tested whether ectodermal gap junction communication was necessary for

mouth opening. When gap junctions were blocked with 0.04% 1-heptanol, which blocks body column shortening (29), no difference in the time history or timescale of mouth opening was observed compared to untreated *Hydra* (**Figure S7b**). These results imply that neither neuronal signaling nor gap junction communication are necessary to coordinate mouth opening once initiated. Instead, mechanical nearest neighbor interactions are sufficient to coordinate and execute mouth opening.

In summary, our model shows how elastic coupling of nearest neighbors can produce a symmetric macroscopic deformation despite stochastic forces acting on a short length scale. By considering different strengths of non-linearity, we demonstrate the role of strain stiffening in tissue mechanics. Strain stiffening is a common phenomenon reported in a variety of tissues (21–24). Our model illustrates how strain stiffening can lead to larger and faster macroscopic deformations. This allows *Hydra* to ingest prey larger than its own diameter and react more quickly to external stimuli.

The model also shows how mechanics alone can be sufficient to coordinate complex, physiologically important behaviors in the absence of neuronal control. It complements recent work in *Trichoplax adhaerens*, a primitive "epithelial" organism that lacks muscles and neurons. In *T. adhaerens*, mechanical forces between epithelial cells have been shown to suffice for maintenance of epithelial integrity in response to external forces. It has been proposed that *T. adhaerens* maintains its epithelial integrity by "active cohesion" - balancing individual cell contractions with local stress softening that prevents detachment of cell-cell junctions (30). In contrast, mouth opening in *Hydra* involves strain stiffening and it begins with loss of epithelial integrity and disruption of cell-cell junctions. Thus, different forms of mechanical coupling could be a fundamental mechanism of generating complex behaviors that evolutionarily precede the neuronal control of behavior. Our study also shows that the rich network of neurons in the *Hydra* hypostome (31,32) may primarily occupy a sensory role as neuronal signaling is only required to trigger mouth opening.

Concluding Remarks

The cigar comb jelly *Beroë* also lacks a permanent mouth and its mechanisms of mouth opening share key similarities with the process we have described in *Hydra*. In both cases, neuronal activity triggers stochastic local contractions which eventually lead to mouth opening (33). Thus, both processes depend on the coordination of local forces to achieve rapid large tissue deformations. How this coordination is achieved depends on the cellular mechanisms of opening: While *Hydra* mouth opening requires the formation of a circular hole in the epithelium originating from the center of the hypostome, *Beroë* mouth opening requires the peeling off of an adhesive strip that holds the two 'lips' of the *Beroë* sealed (33). Both processes are effective solutions for achieving the rapid extreme epithelial deformations that are required for feeding. Studying how these simpler organisms use mechanical nearest neighbor interactions to generate complex behaviors allows us to extract fundamental design principles for tissue bioengineering applications that require extreme deformations of tissue while maintaining structure (as opposed to fluidization of cells as in morphogenesis).

Acknowledgments

The authors thank the Yuste lab for sharing transgenic GCamp6s polyps, Emma Cary and Sharon Fu for help with experiments, Steven Gooden and Kayla Morrill for help with *Hydra* care, Haochen Wang for help with data analysis, Dr. Rui Wang and Dr. Rob Steele for discussions, and Dr. Rob Steele and Dr. Bill Kristan for comments on the manuscript. This work used the Physics Computing Facility at UCSD, and the Strelka Computing Cluster at Swarthmore College. This work was funded by NSF Grant # 2102916 (to EMSC) and US DOE under Award No. DE—FG02—04ER54738 (to PHD). EMA, MC, and JS were supported by the Swarthmore College Interdisciplinary Biology Fellowship. The funders had no role in the design and conduct of the study, in the collection, analysis, and interpretation of the data, and in the preparation, review, or approval of the manuscript.

References

1. Carter JA, Hyland C, Steele RE, Collins EMS. Dynamics of Mouth Opening in Hydra. Biophysical Journal. 2016 Mar 8;110(5):1191–201.
2. Trepat X, Chen Z, Jacobson K. Cell Migration. Compr Physiol. 2012 Oct;2(4):2369–92.
3. Gooshvar S, Madhu G, Ruszczyk M, Prakash VN. Non-Bilaterians as Model Systems for Tissue Mechanics. Integrative and Comparative Biology. 2023 Jun 24;icad074.
4. West DL. The epitheliomuscular cell of hydra: Its fine structure, three-dimensional architecture and relation to morphogenesis. Tissue and Cell. 1978 Jan 1;10(4):629–46.
5. Mueller JF. Some Observations on the Structure of Hydra, with Particular Reference to the Muscular System. Transactions of the American Microscopical Society. 1950;69(2):133–47.
6. Haynes JF, Burnett AL, Davis LE. Histological and ultrastructural study of the muscular and nervous systems in Hydra. I. The muscular system and the mesoglea. Journal of Experimental Zoology. 1968;167(3):283–93.
7. Abrams MJ, Basinger T, Yuan W, Guo CL, Goentoro L. Self-repairing symmetry in jellyfish through mechanically driven reorganization. Proc Natl Acad Sci USA [Internet]. 2015 Jun 30 [cited 2023 Jun 28];112(26). Available from: https://pnas.org/doi/full/10.1073/pnas.1502497112
8. Loomis WF. Glutathione Control of the Specific Feeding Reactions of Hydra. Annals of the New York Academy of Sciences. 1955;62(9):211–27.
9. Aufschnaiter R, Wedlich-Söldner R, Zhang X, Hobmayer B. Apical and basal epitheliomuscular F-actin dynamics during *Hydra* bud evagination. Biology Open. 2017 Jan 1;bio.022723.
10. Szymanski JR, Yuste R. Mapping the Whole-Body Muscle Activity of Hydra vulgaris. Curr Biol. 2019 Jun 3;29(11):1807-1817.e3.
11. Kuo IY, Ehrlich BE. Signaling in Muscle Contraction. Cold Spring Harb Perspect Biol. 2015 Feb 1;7(2):a006023.
12. Wang H, Swore J, Sharma S, Szymanski JR, Yuste R, Daniel TL, et al. A complete biomechanical model of Hydra contractile behaviors, from neural drive to muscle to movement. Proceedings of the National Academy of Sciences. 2023 Mar 14;120(11):e2210439120.
13. Dupre C, Yuste R. Non-overlapping Neural Networks in Hydra vulgaris. Curr Biol. 2017 Apr 24;27(8):1085–97.
14. Forrest H. Lack of dependence of the feeding reaction in hydra on reduced glutathione. The Biological Bulletin. 1962 Jun 1;122(3):343–61.
15. Venturini G. The hydra GSH receptor. Pharmacological and radioligand binding studies. Comparative Biochemistry and Physiology Part C: Comparative Pharmacology. 1987 Jan 1;87(2):321–4.
16. Pierobon P. Regional modulation of the response to glutathione in Hydra vulgaris. Journal of Experimental Biology. 2015 Jul 1;218(14):2226–32.
17. Takahashi T, Hayakawa E, Koizumi O, Fujisawa T. Neuropeptides and their functions in Hydra. Acta Biol Hung. 2008;59 Suppl:227–35.
18. Yum S, Takahashi T, Koizumi O, Ariura Y, Kobayakawa Y, Mohri S, et al. A Novel Neuropeptide, Hym-176, Induces Contraction of the Ectodermal Muscle in Hydra. Biochemical and Biophysical Research Communications. 1998 Jul 30;248(3):584–90.
19. Campbell RD. Elimination by Hydra interstitial and nerve cells by means of colchicine. J Cell Sci. 1976 Jun;21(1):1–13.
20. Tran CM, Fu S, Rowe T, Collins EMS. Generation and Long-term Maintenance of Nerve-free Hydra. JoVE (Journal of Visualized Experiments). 2017 Jul 7;(125):e56115.
21. Trepat X, Grabulosa M, Puig F, Maksym GN, Navajas D, Farré R. Viscoelasticity of human alveolar epithelial cells subjected to stretch. American Journal of Physiology-Lung Cellular and Molecular Physiology. 2004 Nov;287(5):L1025–34.
22. Trepat X, Deng L, An SS, Navajas D, Tschumperlin DJ, Gerthoffer WT, et al. Universal physical responses to stretch in the living cell. Nature. 2007 May;447(7144):592–5.
23. Wang Y, Du Y, Xu F. Strain stiffening retards growth instability in residually stressed biological tissues. Journal of the Mechanics and Physics of Solids. 2023 Sep 1;178:105360.
24. Fernández P, Pullarkat PA, Ott A. A Master Relation Defines the Nonlinear Viscoelasticity of Single Fibroblasts. Biophysical Journal. 2006 May 15;90(10):3796–805.

25. Marcum BA, Campbell RD. Development of Hydra lacking nerve and interstitial cells. Journal of Cell Science. 1978 Feb 1;29(1):17–33.
26. Marcum BA. Culturing Epithelial Hydra. In: Lenhoff HM, editor. Hydra: Research Methods [Internet]. Boston, MA: Springer US; 1983 [cited 2022 Oct 1]. p. 287–90. Available from: https://doi.org/10.1007/978-1-4757-0596-6_38
27. Wood RL. Intercellular Attachment in the Epithelium of Hydra As Revealed by Electron Microscopy. The Journal of Cell Biology. 1959 Dec;6(3):343–52.
28. Fraser SE, Green CR, Bode HR, Gilula NB. Selective disruption of gap junctional communication interferes with a patterning process in hydra. Science. 1987;237(4810):49–55.
29. Takaku Y, Hwang JS, Wolf A, Böttger A, Shimizu H, David CN, et al. Innexin gap junctions in nerve cells coordinate spontaneous contractile behavior in Hydra polyps. Sci Rep. 2014 Jan 7;4:3573.
30. Armon S, Bull MS, Aranda-Diaz A, Prakash M. Ultrafast epithelial contractions provide insights into contraction speed limits and tissue integrity. Proceedings of the National Academy of Sciences of the United States of America. 2018 Oct;115(44):E10333–41.
31. Kinnamon JC, Westfall JA. A three dimensional serial reconstruction of neuronal distributions in the hypostome of a Hydra. Journal of Morphology. 1981;168(3):321–9.
32. Grimmelikhuijzen CJP. Antisera to the sequence Arg-Phe-amide visualize neuronal centralization in hydroid polyps. Cell Tissue Res. 1985 Jul;241(1):171–82.
33. Tamm SL, Tamm S. Reversible Epithelial Adhesion Closes the Mouth of Beroe, a Carnivorous Marine Jelly. The Biological Bulletin. 1991 Dec;181(3):463–73.
34. Glauber KM, Dana CE, Park SS, Colby DA, Noro Y, Fujisawa T, et al. A small molecule screen identifies a novel compound that induces a homeotic transformation in Hydra. Development. 2013 Dec 1;140(23):4788–96.
35. Shimizu H, Koizumi O, Fujisawa T. Three digestive movements in Hydra regulated by the diffuse nerve net in the body column. J Comp Physiol A. 2004 Aug 1;190(8):623–30.
36. Lenhoff HM, Brown RD. Mass culture of hydra: an improved method and its application to other aquatic invertebrates. Lab Anim. 1970 Apr 1;4(1):139–54.
37. Goel T, Wang R, Martin S, Lanphear E, Collins EMS. Linalool acts as a fast and reversible anesthetic in Hydra. PLOS ONE. 2019 Oct 24;14(10):e0224221.

Figures and Tables

Figure 1: *Hydra* head anatomy and mouth opening dynamics. (a) Schematic showing basic *Hydra* anatomy and cell types including a zoomed-in cross-section of the hypostome. (b) Schematic top-down view of the myoneme organization in the ectoderm (green) and endoderm (magenta) in the *Hydra* head. (c) Area of the mouth (normalized to the maximum

area) as a function of time. The blue curve shows representative experimental data. The black curve corresponds to a logistic fit as described by the equation on the right. 'a', 'b', 'c' and 'd' correspond to the minimum normalized area, maximum normalized area, time to reach half maximum and timescale of mouth opening respectively. (d) Still images from **Movie S1** showing quinine hydrochloride (0.5 mM) induced opening of the ectodermal epithelial layer in a Watermelon (WM) *Hydra* (scale bar: 100 μm). (e) Histogram of number of cells involved in each tugging event (n = 364 tugging events from N = 8 independent events). (f) Probability density function for the relative angle between successive tugging events (n = 184 tugging event pairs from N = 5 independent mouth opening events). (g) Representative image of a radial tug during mouth opening induced by 0.2mM reduced glutathione (scale bar: 200 μm). (h) Time evolution of the relative fluctuation of the mouth radius, δr/r, averaged over the azimuth (N = 6 mouth opening events). Time is normalized from the beginning of mouth opening to when the mouth reaches its maximum area.

Figure 2: Non-linear spring network model captures macroscopic features of mouth opening. (a) Schematic of the spring network. Color-coding indicates distance from center. (b) Comparison between mouth opening time series obtained from model simulations (blue) and the logistic curve fit (red). Intensity of grey background denotes phases of mouth opening (from light to dark): slow increase, fast increase, and saturation. (c) Azimuthally averaged radial deformation of vertices in each N-gon. Line colors match those of the radial springs in (a). Grey background matches that of (b). (d) Variation of final mouth area (left column) fitted mouth opening time (middle column), and relative fluctuations in mouth radius, δr/r (right column), as functions of the active force strength (x-axis) and the average forcing rate (y-axis) for different non-linear regimes: without non-linearity (top), weak non-linearity (middle) and strong non-linearity (bottom). Note the axes have logarithmic scales. A darker blue color indicates larger mouth areas (left), longer opening times (middle) and larger relative fluctuations in mouth radius (right). (e) Changes in relative fluctuations in mouth radius with changes in the stiffness of the azimuthal springs relative to stiffness of radial springs (κ_0). $l_0 = 30\ \mu m$ for all three heat maps. Parameters for all simulations along with descriptions and relevant sources can be found in **Table S1.**

Figure 3: Application of external uniaxial tension affects symmetry of mouth opening. (a) Schematic of the hypostome under uniaxial tension. F_{asp} is the strength of the microaspiration force. (b) Still image sequence of mouth opening when the head is placed under uniaxial tension by applying negative pressure. Arrowheads indicate the location of needles used to apply negative pressure on the head. Star indicates the mouth opening (Scale bar: 100 μm). (c) Orientation angle of major axis (relative to the direction of tensile force) and (d) aspect ratio of best fit ellipse to the mouth, in simulations, as functions of the strength and rate of the active force ($l_0 = 20\mu m$). (e) Orientation angle of major axis (relative to the direction of tensile force) (N = 13) and (f) aspect ratio of best fit ellipse to the mouth, from experiments (N = 9 (Control), N = 13 (Microaspirated)). (*) indicates p-value = 0.0006 for a one-tailed two-sample Student's *t*-test.

Figure 4: The nerve-net is required to initiate but not to execute mouth opening. (a) Schematic of the simulated chimera. (b) Greyscale images of innervated and nerve-free *Hydra* generated by heat shock treatment of the A10 strain. Note the nerve-free animal is more bloated at the oral end due to buildup of fluid. (c) Schematic showing the process of creating chimeras. (d) Still image sequence of mouth opening in an innervated:nerve-free chimera (scale bar: 100 μm). Representative mouth area-time curves (e) *in vivo* and (f) *in silico*. Comparison of the (g) ratio of mouth opening times and (h) relative fluctuations in mouth radius between control chimeras (N = 6) and innervated:nerve-free chimeras (N = 9). (*) denotes p-value < 0.05 (i) Ratio of mouth opening times and (j) relative fluctuations in mouth radius for innervated:nerve-free chimeras, in simulations, as functions of the strength and rate of the active force in the strongly non-linear regime ($l_0 = 10\mu m$). Simulation parameters provided in **Table S1**.

Materials and Methods

Model Description

The epithelial tissue of the hypostome is modeled as a system of (R+1) concentric regular N-gons (polygons with N vertices), all lying in the same plane. Each vertex is connected to its topological nearest neighbors (so each vertex is connected to 4 others, except the ones on the innermost and outermost polygon) by a non-linear spring (**Figure 2a**). All vertices, except those in the $(R+1)^{th}$ polygon are movable. The $(R+1)^{th}$ polygon represents a fixed boundary, mimicking the role of the tentacle ring in the hypostome. For each movable vertex, we can write the momentum balance equation:

$$\frac{d\vec{r}_{i,j}}{\mu dt} = -\left\{\kappa(\|\vec{r}_{i,j}-\vec{r}_{i-1,j}\|-a)+\frac{\kappa}{l_0^2}(\|\vec{r}_{i,j}-\vec{r}_{i-1,j}\|-a)^3\right\}\frac{\vec{r}_{i,j}-\vec{r}_{i-1,j}}{\|\vec{r}_{i,j}-\vec{r}_{i-1,j}\|}$$

$$-\left\{\kappa(\|\vec{r}_{i,j}-\vec{r}_{i+1,j}\|-a)+\frac{\kappa}{l_0^2}(\|\vec{r}_{i,j}-\vec{r}_{i+1,j}\|-a)^3\right\}\frac{\vec{r}_{i,j}-\vec{r}_{i+1,j}}{\|\vec{r}_{i,j}-\vec{r}_{i+1,j}\|}$$

$$-\left\{\kappa(\|\vec{r}_{i,j}-\vec{r}_{i,j-1}\|-b_i)+\frac{\kappa}{l_0^2}(\|\vec{r}_{i,j}-\vec{r}_{i,j-1}\|-b_i)^3\right\}\frac{\vec{r}_{i,j}-\vec{r}_{i,j-1}}{\|\vec{r}_{i,j}-\vec{r}_{i,j-1}\|}$$

$$-\left\{\kappa(\|\vec{r}_{i,j}-\vec{r}_{i,j+1}\|-b_i)+\frac{\kappa}{l_0^2}(\|\vec{r}_{i,j}-\vec{r}_{i,j+1}\|-b_i)^3\right\}\frac{\vec{r}_{i,j}-\vec{r}_{i,j+1}}{\|\vec{r}_{i,j}-\vec{r}_{i,j+1}\|}$$

$$+\delta_{i,R}\tilde{f}_0\sum_n\frac{1}{\sqrt{2\pi\sigma^2}}e^{-\frac{(t-t_n)^2}{2\sigma^2}}\frac{\vec{r}_{i+1,j}-\vec{r}_{i,j}}{\|\vec{r}_{i+1,j}-\vec{r}_{i,j}\|}$$

$$t_n \sim Poiss(\lambda)$$

$$\frac{d\vec{r}_{R+1,j}}{\mu dt} = 0$$

where, $\vec{r}_{i,j}$ is the position of the vertex in the *i*-th N-gon at the *j*-th azimuthal position at time t. a is the rest length of the radial springs. b_i is the rest length of the azimuthal springs in the i-th N-gon. κ is the spring constant, μ is the coefficient of mobility and l_0 is the length at which the linear and non-linear forces are of equal magnitude. $\delta_{i,R}$ is the Kronecker delta function, $\tilde{f}_0$ is the strength of the active force, σ is the duration over which the force acts and t_n is the time at which the force acts. t_n are drawn randomly from a Poisson distribution with a mean rate λ.

The initial positions of the vertices are:

$$\vec{r}_{i,j} = (a_0 + (i-1)a)\left(cos\left(\frac{2\pi j}{N}\right)\hat{x} + cos\left(\frac{2\pi j}{N}\right)\hat{y}\right)$$

a_0 is the initial radius of the mouth, equal to one cell radius. Also,

$$b_i = 2(a_0 + (i-1)a)sin\left(\frac{\pi}{N}\right)$$

The values of all these parameters are provided in **Table S1**. To model the microaspiration experiment, we added an additional constant radial force (**Table S1**) and to model the chimera we set the active force to zero at specific vertices (see Supplemental Appendix Section 1.5).

Numerical methods

The model equations were solved using custom MATLAB 2021a (MathWorks) scripts. For each set of free parameters, 5 realizations of the stochastic external force were simulated. The system of coupled ODEs described in the model description section were then solved for each realization using a 4th order Runge-Kutta scheme. For each realization, the final area of the mouth, and the azimuthal average and standard deviation of mouth radius were obtained. The timescale of mouth opening was obtained by fitting the mouth area from the simulations to the experimentally obtained logistic curve using a linear least squares approach. Realizations which generated unphysical results (leading either to mouth areas orders of magnitude larger than the rest of the realizations or mouth opening timescales less than 50ms) were discarded. The outputs from the remaining realizations were then averaged for each set of parameters. The relevant code is available on Zenodo (see **Software S1** for the link**)**.

***Hydra* strains and culture**

The *Hydra vulgaris* AEP strain and various transgenic lines derived from this strain: Epithelial GCaMP, expressing GCaMP6s in the ectoderm (10); HyBra, expressing GFP under control of the HyBra2 promoter:GFP transgenic animals (34); "Watermelon" (WM) animals (34) expressing GFP in the ectoderm and DsRed2 in the endoderm with both genes under control of an actin gene promoter; Lifeact-GFP strains (9), expressing Lifeact-GFP under the control of the *Hydra actinI* promoter, in the ectoderm or in the endoderm and, *Hydra vulgaris* strain A10 (chimera consisting of *Hydra vulgaris* (formerly *Hydra magnipapillata* strain 105) epithelial cells and sf-1 interstitial cells, which are temperature sensitive interstitial cells (35) were used for experiments. *Hydra* strains were maintained in mass cultures in *Hydra* medium (HM) composed of 1 mM $CaCl_2$ (Spectrum Chemical, Cat#C1096-500GM), 0.1 mM $MgCl_2$ (Sigma-Aldrich, Cat#M0250-1KG), 0.03 mM KNO_3 (Fisher Scientific, Cat#P263-500), 0.5 mM $NaHCO_3$ (Fisher Scientific, Cat#S233-500), and 0.08 mM $MgSO_4$ (Fisher Scientific, Cat#BP213-1) prepared with MilliQ water, with a pH between 7 and 7.3. Cultures were maintained at 18°C in the dark in a Panasonic incubator (Panasonic MIR-554, Tokyo, Japan). The cultures were fed 2-3x/week with *Artemia* nauplii (brine shrimp) from the San Francisco Bay or from the Great Salt Lake (Brine Shrimp Direct). Animals were cleaned daily using standard cleaning procedures (36). Asexual, non-budding polyps starved for at least 24 hours were used for experiments unless stated otherwise.

Calcium signaling in mouth opening

The large-scale tissue deformation of mouth opening prevents the resolution of individual myonemes **(Figure S2)**. Therefore, we visualized myoneme activation indirectly by imaging transgenic strains with calcium reporters in the ectoderm (10), using calcium signaling as a proxy for cell activity. Additionally, we quantified the consequences of myoneme activation by measuring changes in cell shapes. Combining these data, we were able to infer the length scale associated with individual myoneme contractions and the timescale over which local myoneme contractions are independent of each other.

Epithelial GCaMP polyps, expressing GCaMP6s in the ectoderm, were starved for 24-72 hours before imaging. Movies were recorded on the Olympus IX81 inverted microscope (Olympus Corporation) equipped with an Zyla sCMOS camera (Andor Technology-Oxford Instruments), an X-cite Xylis (Excelitas, Model#XT720L) fluorescence light source, and Slidebook 2022 software (Intelligent Imaging Innovations). For top-down imaging, *Hydra* were decapitated just below the tentacle ring in 1mM linalool (37) (Sigma-Aldrich, Cat#L2602-100G), rinsed in HM, and allowed to heal for 1-2 hours before imaging. *Hydra* polyps (for side-view imaging) or heads (for top-down imaging) were mounted on 75 x 25 mm glass slides (Corning, Cat#2949-75X25) in a few drops of 1mM linalool (Sigma-Aldrich) for side-view imaging or HM for top-down imaging. Double-sided tape was used as a spacer. Due to the different thicknesses of different brands, as well as different sizes of *Hydra* polyp heads and body columns, the amount of tape used varied. For side-view imaging, two pieces of Amazon Basic tape usually sufficed, while 3 pieces of Scotch tape worked equally well. For top-down imaging of heads, one piece of Scotch double-stick tape spaced with an additional small rectangle cut from a Kimwipe (Fisher Scientific, Cat#06-666A) was used. A 22x22 mm glass coverslip (Fisher Scientific, Cat#12-542-B) was overlayed such that there was an opening on one side of the glass slide. Mouth opening was induced by adding 80 µL of 0.5-2.0 mM (-)-quinine hydrochloride dihydrate (Sigma-Aldrich, Cat#22630-10G-F) or 0.1-0.5 mM reduced L-glutathione (Sigma-Aldrich, Cat#G4251-10G) through one open end of the tunnel slide while a Kimwipe (Fisher Scientific) was held at the other end to absorb any extra fluid. Stock quinine solution was protected from light using aluminum foil, and both reduced glutathione and quinine stock solutions were made fresh weekly and stored at 4°C. Side-view images were recorded using a 4×/0.13 UPlanFL N objective (Olympus Corporation), while top-down images were recorded using a 20×/0.45 LUCPlanFL N objective (Olympus Corporation). Both sideview and top-down images were recorded with frame rates of 10-20 fps, 2x2 binning and 100% fluorescence intensity.

Microaspiration experiment

Microaspiration needles were prepared as described in the Supplemental Text.

Large, 2-3 day starved, WM *Hydra* were decapitated at least 1hr before imaging as follows: polyps were first incubated in 1mM linalool (Sigma-Aldrich) for 10 minutes and decapitated and the tentacles removed at their base. Samples were then washed once in HM and incubated at room temperature for 1-2 hrs to allow for wound healing and for the linalool to wear off.

A 6 mm glass concavity slide was propped up and positioned under the Leica MZ16FA microscope and filled with HM. The left and right micromanipulators were positioned such that the needle was immersed in the HM in the glass well. Aspiration was achieved by suctioning water through the tube by gently pulling the syringe plunger until approximately 1 mL of HM was inside the syringe, then removing the plunger entirely, and positioning the syringe so that the water level in the syringe was lower than that of the concavity slide. Once both the left and right microaspirators were experiencing negative pressure and needles were aligned approximately 180° to each other and within camera view, fluorescence was turned on using the GFP2 filter, the brightfield decreased, and the needles were pulled out of camera view. A *Hydra* head was then placed in the center of the glass well, between the needles. The head was then positioned hypostome-up. Final positioning of the hypostome was achieved with the aid of a hair loop. The left and right microaspirators were then positioned to suction the head, approximately 180° apart. Once so positioned, the microaspirators were adjusted such that the needles pulled the head to distort it from circular symmetry. The height of the water in the syringe relative to the concavity well was recorded. Enough water was removed from the dish to minimize image distortions, while maintaining negative pressure. Bright field was then turned off entirely and a NIGHTSEA SFA light head BNC (Stellar Scientific) was positioned to shine light directly on the *Hydra*

554 head. Images were recorded on the Leica MZ16FA microscope using a Leica 10445930 1.0x stereo
555 microscope C-mount camera adapter connected to a Point Grey Grasshopper3 camera at a rate of 2 fps using
556 the Flycapture2 Software (Point Grey). Mouth opening was induced by sequentially adding 80 µL of 0.5 mM,
557 1.0 mM, 1.5 mM, and 2.0 mM (-)-quinine hydrochloride dihydrate (Sigma-Aldrich) to the concavity well
558 until mouth opening was observed.
559
560 Data sets were discarded for samples in which the hypostome was permanently distorted or damaged after
561 the microaspiration. As a control, we tested whether the symmetry of the mouth opening was affected by
562 physical contact of the needle with the tissue in the microaspiration setup. This was achieved by fixing only
563 one side of the *Hydra* head by one microaspirator needle at low pressure and inducing opening. For the
564 control analysis two types of heads were used: 5 heads post-microaspiration experiment and 4 new heads.
565 The means of the aspect ratio of the mouth openings for the two types of control heads (post-microaspiration
566 v. new) were not found to statistically differ ($p = 0.56$ two-sample Student's *t*-test MATLAB).
567
568 **Generation and imaging of innervated:nerve-free chimera**
569 Nerve-free (NF) A10 and innervated HyBra were used to generate chimeras with half of the hypostome
570 innervated and the other half nerve-free. Only NF A10 polyps that had the bloated body column phenotype
571 (20), were unable to open their mouths to feed and were similar in size to the HyBra polyps were selected.
572 The chosen NF A10 and HyBra polyps were put in a dish containing 1.25% methyl cellulose (Acros Organics,
573 Cat#258111000) and 1 mM linalool (Sigma-Aldrich) in HM for 10 min. Each polyp was then decapitated
574 one-third of the way down the body column with a scalpel. The resulting head pieces were each prompted to
575 open their mouth with a tap of the forceps, and a lateral cut across the hypostome and tentacles was made
576 with the scalpel to bisect the mouth. The half hypostome pieces were matched with the opposite *Hydra* strain
577 piece and grafted together: Glass needles were pulled from 5 µL microcapillaries (Corning Inc.) over a
578 Bunsen burner to a thickness of around 0.03 mm. The hypostome pieces were then strung onto the needle
579 and a small square of Kimwipe (Fisher Scientific) was placed on either side of the grafted pieces to ensure
580 they stayed in contact during healing. These chimeras were allowed to heal on the needle for 1.5 h in the
581 methyl cellulose solution and were then removed from the needle with forceps. The chimeras were transferred
582 to a new dish with HM and allowed to heal overnight (between 14 and 24 h) in the 18°C incubator. Any
583 leftover body column tissue was cut off from the chimeras using a scalpel. The chimeras were incubated in
584 a solution of 1:1000 (wt:vol) 1-aminoanthracene (Sigma Aldrich, Cat#A38606) for 7 min in the dark to
585 provide a temporary green fluorescence, then washed three times with HM. Once stained, chimeras were kept
586 in the dark and imaged on the EVOS FL Auto 2 microscope equipped with a 10×/0.3 Plan Fluor objective.
587 Mouth opening events were either spontaneous (not induced by external stimuli) or induced by adding 0.5-
588 1.5 mM (-)-quinine hydrochloride dihydrate (Sigma-Aldrich) or 0.1-0.5 mM reduced L-glutathione (Sigma-
589 Aldrich). Images were recorded at framerates between 10-22 fps.
590 To account for possible effects on behavior due to strain differences, we performed control experiments with
591 chimeras containing innervated A10 and HyBra using the same protocol, except for the fact that innervated
592 A10 animals were used in place of the NF A10.

593 RFamide antibody staining was used to confirm the absence of neurons in the nerve-free tissue of the
594 chimeras after imaging (**Figure S7a**). The chimeras were fixed with 4% paraformaldehyde (Ted Pella, Inc,
595 Cat#50-00-0) made in HM. Chimeras were first relaxed in 1 mM linalool (Sigma-Aldrich) for 5 min, then
596 transferred to the paraformaldehyde solution and fixed for 1 hr at room temperature or overnight at 4°C in
597 the dark. Samples were then washed once quickly with 0.3% PBSTx (0.3% Triton-X (Sigma-Aldrich,
598 Cat#T9284) in 1x PBS (MP Biomedicals Inc, Cat#092810306), followed by two 5 min washes. The fixed
599 chimera samples were placed on glass slides for a wet mount antibody stain. Humid chambers for staining

were constructed by lining covered 100 mm Petri dishes (Spectrum Scientific, Cat#961-62084) with wet paper towels and placing the slides inside the dishes. A well was created in the center of each glass slide by layering two pieces of double-sided tape across both short sides of the slide with one piece of tape running on both long edges of the slide. The samples were placed in a drop of HM on the slide. All steps were performed at room temperature unless noted otherwise. The samples were washed three times with 20 μL 1x PBS (MP Biomedicals), followed by a 15 min permeabilization with 20 μL 0.5% PBSTx. They were then incubated for 3.5 h in 20 μL blocking solution (10% FBS (Sigma-Aldrich, Cat#F6178), 1% DMSO in 1x PBS) and placed overnight (16 h) at 4°C in 30 μL anti-RFamide primary antibody (gift from Dr. Kathleen Siwicki) diluted 1:200 in the blocking solution. On the second day, samples were washed quickly 3x with 40 μL 1x PBS, followed by four 30-minute washes of 20 μL 0.3% PBSTx. The samples were then incubated in a 1:1000 or 1:500 dilution of Alexa 488 Goat anti-rabbit IgG secondary antibody (Thermo-Fisher Scientific, Cat#A-11008) for 5 h, followed by three quick and two 10 min washes of 0.3% PBSTx. The samples were then washed three times with 1x PBS. The 1x PBS was replaced with a 1:1 solution of glycerol (Omnifur, Cat#4750) and HM. Finally, a coverslip was placed over the samples and nail polish was used to seal the slides. Z-stacks of the samples were imaged using a Leica high-resonance scanning SP5 confocal microscope with a 20x C-Apochromat 1.2 W objective.

Mouth opening after heptanol treatment

Two-day starved *Hydra* were decapitated under a dissection scope using a scalpel and allowed to heal for 1 hr in HM at room temperature. The heads, along with a whole *Hydra* were incubated in 0.04% 1-heptanol (Acros Organics, Cat#120362500). The solution was prepared by adding 4 µL of heptanol to 10 mL HM. The whole *Hydra* polyps were pinched using forceps to ensure that body column contractions had been inhibited and therefore, gap junctions had been blocked (14). The incubated heads were then mounted on 75 x 25 mm glass slides (Corning) in the heptanol solution and covered using 22x22 mm glass coverslips (Fisher Scientific) with layers of double-sided tape as spacers. Mouth opening was either spontaneous or induced using 0.5 mM quinine hydrochloride (Sigma-Aldrich) prepared in the 0.04% 1-heptanol solution. Images were recorded using the Olympus IX81 inverted microscope (Olympus Corporation) equipped with a 10x/0.40 UPlanSApo objective and an Orca-ER charge-coupled device camera (Hamamatsu Photonics) using SlideBook software (Intelligent Imaging Innovations). Movies were analyzed to extract the timescale of opening (the d-parameter) as described in the "quantification and statistical analysis" section.

QUANTIFICATION AND STATISTICAL ANALYSIS

Mouth opening shape and area as functions of time

Custom MATLAB scripts (MATLAB 2021a, Mathworks) were used to obtain the area of the mouth across several frames, as described in (1). Briefly, single channel images of the mouth were first binarized. A polygonal region was manually identified as the mouth in the first image of the sequence. Successive images were thresholded based on the pixel intensities in the polygonal region to identify the mouth. For each frame, once the mouth boundary was identified, the area of the mouth, major and minor diameters of the best fit ellipse, and the mean and standard deviation of the mouth radius were calculated.

The areas were then normalized so that they range between 0 and 1. The normalized areas were plotted as a function of time and fit to the logistic equation below using linear least squares fit.

642

643 $$A(t) = a + \frac{b}{1 + e^{-\left(\frac{t-c}{d}\right)}}$$

644

645 **Analysis of local contractions and mouth symmetry**

646 We binned the mouth opening movies into 100 ms intervals and quantified the relative angle between
647 successive tugging events (as defined in **Figure 1f,g**). Using a 2-sample Kolmogorov Smirnov test, we
648 found that the probability density of the angles is not significantly different from a uniform distribution. We
649 also tracked the relative fluctuations (over the azimuth) in the radius of the mouth at its maximum area.
650 This ratio is essentially a measure of the asymmetry of the mouth shape. The relative fluctuations were
651 calculated by dividing the standard deviation in the radius of the mouth by the average radius, measured
652 when the mouth was at its maximum area.

653

654 **Analyzing mouth openings in microaspiration experiments**

655 Mouth openings were analyzed manually using FIJI. In each recorded video, the frame with the largest
656 mouth opening (the frame of interest) was first identified. To do so, the approximate frame of interest was
657 found by visual inspection. Then, the mouth areas in this frame and +/- 5 neighboring frames were
658 measured using the polygon tool. If the mouth area was largest in this frame of interest, it was selected for
659 further analysis. If not, the frame with the largest mouth area was selected as the approximate frame of
660 interest and the mouth areas in its neighboring frames were measured. This process was repeated until the
661 frame of interest was found.

662 Only videos in which heads did not appear damaged after microaspiration were included in analysis. For
663 movies in which multiple mouth openings occurred, the largest mouth opening frame was chosen for
664 analysis. The frame of interest from each video was independently analyzed by four researchers, two of
665 which were "blind" and knew nothing of the expected outcome for the shape of mouth opening in
666 microaspirated heads. All researchers had access to the raw images.

667 The frame of interest was analyzed as follows: A line was drawn connecting the center of the needles on
668 each side of the *Hydra* head (or for the control: from the center of one needle to the center of the mouth),
669 from which the angle to the image horizontal (θ_1) was recorded. The perimeter of the mouth was then
670 traced using the polygon tool, from which the ellipse major, the ellipse minor, and the angle of the ellipse
671 to the horizontal (θ_2) were recorded. The relative angle $\theta_{Rel} = |\theta_2 - \theta_1|$ was calculated and recorded,
672 taking care to account for symmetry such that $\theta_{Rel} \leq 90^\circ$. The relative angle is plotted in **Figure 3f**. The
673 major to minor aspect ratios for the 13 microaspirated and 9 control heads were determined and were each
674 found not to differ significantly from a normal distribution (p-value = 0.18 (microaspirated), p-value = 0.66
675 (control), two-sample Kolmogorov Smirnov test against a uniform distribution MATLAB 2021a
676 (MathWorks)). Microaspirated heads and control heads were statistically compared by evaluating the p-
677 value from a two-sample one-tailed Student's *t*-test. The suction pressure (P) on the left (L) and right (R)
678 sides of the *Hydra* head was calculated by the formula $P_{L/R} = \rho g \Delta h_{L/R}$, where ρ is the density of water, g
679 is the acceleration due to gravity, and Δh is the height difference between the water level in the syringe to

680 the bottom of the glass well containing the *Hydra* head. The cross-section areas of the needles were
681 calculated from the recorded radii. Finally, the total suction force ($F_{L/R}$) on each side of the hypostome was
682 calculated by multiplying the suction pressure by the cross-section area of the needle.

683

684 **Analyzing mouth openings in innervated:nerve-free chimera**
685 Mouth openings in chimeras were analyzed manually using FIJI. The line tool was
686 used to demarcate the segments of the mouth opening enclosed by the innervated (or nerve-free)
687 half. The polygon tool was then used to enclose each segment of the mouth opening and
688 obtain their areas. The areas of the nerve-free and the innervated segments of the mouth were
689 individually normalized to their respective maximum areas, so the areas lay between 0 and 1.
690 The normalized areas of the innervated and nerve-free halves were plotted against time and
691 individually fit to the logistic equation to obtain the timescales of mouth opening
692 (the 'd' parameter). The ratio of the d parameters for the A10 and HyBra halves was calculated
693 for each chimera.